PCCP

ROYAL SOCIETY OF CHEMISTRY

PAPER

View Article Online
View Journal | View Issue

Check for updates

Cite this: *Phys. Chem. Chem. Phys.*, 2024, **26**, 13152

Synergistic effect between $ZnCo_2O_4$ and Co_3O_4 induces superior electrochemical performance as anodes for lithium-ion batteries

Anubha Tomar,†[a] Zulkifli, †[b] Jay Singh,[a] Satendra Pal Singh,[c] Jaekook Kim *[b] and Alok Kumar Rai *[a]

Received 19th December 2023,
Accepted 23rd March 2024

DOI: 10.1039/d3cp06156f

rsc.li/pccp

The current work describes a facile synthesis of spinel-type $ZnCo_2O_4$ along with an additional phase, Co_3O_4, by simply maintaining a non-stoichiometric ratio of Zn and Co precursors. Pure $ZnCo_2O_4$ and Co_3O_4 were also synthesized using the same method to compare results. The obtained morphologies of samples show that small-sized nanoparticles are interconnected and form a porous nanosheet-like structure. When used as anode materials for Li-ion batteries, the $ZnCo_2O_4/Co_3O_4$ nanocomposite electrode exhibits a highly stable charge capacity of 1146.2 mA h g^{-1} at 0.5C after 350 cycles, which is superior to those of other two pure electrodes, which can be attributed to its optimum porosity, synergistic effect of $ZnCo_2O_4$ and Co_3O_4, increased active sites for Li^+ ion diffusion, and higher electrical conductivity. Although the pure Co_3O_4 electrode displayed a much higher rate capability than the $ZnCo_2O_4/Co_3O_4$ nanocomposite electrode at all investigated current rates, the Co_3O_4 morphology apparently could not withstand long-term cycling, and the electrode became pulverized due to the repeated volume expansion/contraction, resulting in a rapid decrease in the capacity.

Published on 05 April 2024. Downloaded on 3/4/2026 1:21:38 AM.

1 Introduction

Transition metal oxides have been widely studied as promising anode materials to replace the conventional anode graphite, whose theoretical capacity is much inferior (only ~372 mA h g^{-1}), due to the growing demand for large-scale energy storage devices. Since transition metal oxides exhibit great promise, such as earth abundance, large specific capacity, suitable discharge voltages and synthetic versatility, it is believed that they might fulfill the immediate demands of advance LIB applications. In particular, the binary metal oxide Co_3O_4 possesses various intriguing features, such as high theoretical capacity (~890 mA h g^{-1}), good thermal/chemical stability, excellent catalytic activity, easy production, low toxicity and high redox activity.[1–10] However, Co_3O_4 unfortunately has numerous issues including poor ionic and electronic conductivity and drastic volume expansion/contraction during charge/discharge, resulting in unsatisfactory rate performance and unstable cycling performance, which ultimately restricts its commercial applications in LIBs.[11,12] Among various strategies that have been adopted to overcome the above issues of Co_3O_4 anodes, the fabrication of nanoscale porous architectures with tailored morphology was suggested as an effective method to reduce the diffusion path length of ions and buffer volume variations that occur during the Li^+ insertion/de-insertion process.[2,13–20] However, this proposed strategy was also unable to provide Co_3O_4 anodes with excellent electrochemical performance.[15] Thereafter, a novel research effort was made to fabricate ternary metal oxide anodes by partially replacing the cobalt (Co) of Co_3O_4 using various elements to alleviate above-mentioned issues *via* the complementary behavior and synergistic effect between the two different metal elements.[21,22] Among all ternary metal oxides, the synthesis and/or use of $ZnCo_2O_4$ spinel has been abundantly reported for energy conversion and storage applications due to its low cost, low toxicity, numerous novel morphologies, excellent electrical conductivity, high theoretical capacity (~903 mA h g^{-1}) and use of inexpensive and nontoxic Zn.[23–26] In addition, the conversion and alloying/de-alloying reactions occurred in the $ZnCo_2O_4$ anode because of the further reaction of Zn as a conversion product with Li and formation of the LiZn alloy, which eventually offers extra capacity.[23] However, like other anodes, $ZnCo_2O_4$ suffers from intrinsically low conductivity and large volume variations (~200%) during the lithium insertion/de-insertion process, resulting in electrode cracking, poor cycling stability and low rate capability.[27] Recently, it was reported that the framing of

[a] *Department of Chemistry, University of Delhi, Delhi-110007, India. E-mail: akrai@chemistry.du.ac.in*
[b] *Department of Materials Science and Engineering, Chonnam National University, 300 Yongbong-dong, Bukgu, Gwangju, 500-757, Republic of Korea. E-mail: jaekook@chonnam.ac.kr*
[c] *Department of Physics, University of Lucknow, Lucknow 226007, India*
† These authors contributed equally to this paper.

This journal is © the Owner Societies 2024

Published on 05 April 2024. Downloaded on 3/4/2026 1:21:38 AM.

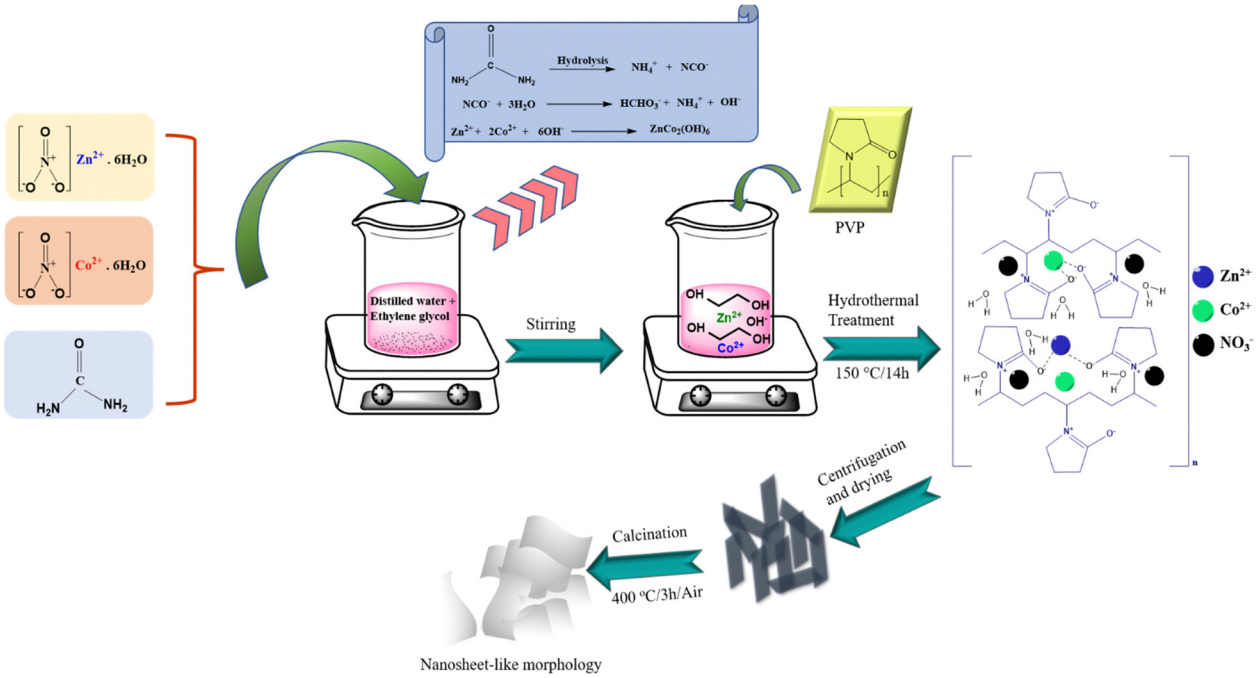

Scheme 1 Schematic illustration of the synthesis of the $ZnCo_2O_4$ sample.

two different active materials in one frame was found to be promising to improve physical/chemical properties and provide high electrochemical reactivity and excellent mechanical stability due to the synergistic effect of each component.[7–10] Since $ZnCo_2O_4$ and Co_3O_4 individually exhibit severe limitations as an anode for LIBs, it would be novel to manufacture a single advanced electrode that combined the characteristics of the electrodes by offering high capacity due to the contribution of each electrode and that nullified their individual limitations during repeated charge/discharge cycles. Although Zn and Co have electrochemical activity toward lithium, their mutual favorable buffering matrices and complementary behavior may not only alleviate the large mechanical stress derived from the severe volume change during cycling but also contribute to enhancing the lithium-storage performance.

Thus, in the current work, a nanocomposite of $ZnCo_2O_4$ and Co_3O_4 was synthesized by simply controlling the molar ratio of the Zn and Co precursors. It is believed that the $ZnCo_2O_4/Co_3O_4$ nanocomposite electrode may exhibit superior electrochemical performance due to the intimate interconnection between $ZnCo_2O_4$ and Co_3O_4, which can relieve stresses caused by volume variations due to the different working voltages of the two electrochemically active metal oxides. Additionally, the coexisting Co_3O_4 may participate in electrochemical reactions and contribute to the total capacity of the host material by storing $8Li^+$ ions per formula unit ($Co_3O_4 + 8Li^+ + 8e^- \leftrightarrow 3Co + 4Li_2O$).

2 Experimental

2.1 Materials and methods

Scheme 1 presents a schematic illustration of the synthesis procedure that was used to prepare the samples. In a typical synthesis, 0.3 g of urea and nonstoichiometric amounts of the precursors, namely, 2 mM zinc nitrate ($Zn(NO_3)_2{\cdot}6H_2O$, Sigma Aldrich, 98%, Germany) and 6 mM cobalt(II) nitrate hexahydrate ($Co(NO_3)_2{\cdot}6H_2O$, Sigma Aldrich, ≥98%, United Kingdom) were first combined. Then, all reagents were dissolved in a mixed solution of 40 mL of deionized water and 30 mL of ethylene glycol (EG) under constant stirring at room temperature. Thereafter, 0.5 g of polyvinyl pyrrolidone (PVP, M_w = 40 000 g mol^{-1}, Alfa Aesar, China) was added to the above solution under continuous magnetic stirring to achieve a homogeneous solution. Then, the obtained homogeneous solution was transferred into a 100-mL Teflon-lined stainless-steel autoclave and heated to 150 °C for 14 h. After natural cooling to room temperature, the as-obtained product was washed with de-ionized water and absolute ethanol several times and later dried in an oven at 60 °C overnight. The dried product was further calcined at 400 °C for 3 h in air, with a ramping rate of 2 °C min^{-1} to ensure the purity of the sample. For comparison, pure $ZnCo_2O_4$ was synthesized with same experimental conditions except using a Zn : Co stoichiometric ratio of 2 : 4. In addition, pure Co_3O_4 was synthesized using same parameters but without the precursor $Zn(NO_3)_2{\cdot}6H_2O$.

2.2 Material characterization

To confirm the crystal structure and phase purity of calcined products, X-ray diffraction (XRD) analysis was performed using a Bruker D8 discover high-resolution X-ray diffractometer with Cu Kα radiation (λ = 1.5406 Å, Karlsruhe, Germany). Detailed microstructural analysis was carried out using field-emission scanning electron microscopy (FE-SEM, Zeiss Gemini SEM 500 Thermal field emission type, Zeiss) equipped with energy dispersive spectrometry (EDS) and field emission transmission electron

Published on 05 April 2024. Downloaded on 3/4/2026 1:21:38 AM.

microscopy (FE-TEM, FEI Tecnai G2-20 at 200 kV). The specific surface area of calcined samples, including the pore size distribution, was determined using the Brunauer–Emmett–Teller (BET, Micromeritics Instrument Corp. Gemini-V) using the N_2 adsorption/desorption isotherm. X-ray photoelectron spectroscopy (XPS) was also used to investigate the chemical composition and oxidation states of the elements present in the samples using M/s Thermo Fischer Scientific Instrument UK with a monochromatic Al Kα X-ray source.

2.3 Electrode fabrication

CR2032 coin-type half-cells were fabricated using lithium metal foil as the counter and reference electrode to measure the electrochemical properties of the calcined samples. The slurries were first prepared by mixing of 60 wt% of the active material, 20 wt% of carbon black as a conductive agent and 20 wt% of polyvinylidene difluoride (PVdF) as a binder in *N*-methyl-2-pyrrolidone (NMP). The obtained paste was then cast on a copper foil (current collector) using a doctor blade, which was then dried in a vacuum oven at 120 °C overnight and pressed through a twin roller hot press for better contact between the copper foil and slurry. The cell assembly was then performed in an argon (Ar)-filled glovebox (H_2O and O_2 content less than 1 ppm). Glass fibre was used as a separator. A 1 M solution of the salt $LiPF_6$ in an ethylene carbonate (EC) : dimethyl carbonate (DMC) mixture with a volume ratio of 1 : 1 was used as the electrolyte. The electrochemical testing of assembled half-cells was performed using a BTS-2004H, Nagano, Japan electrochemical workstation within the potential range of 0.01–3.0 V *vs.* Li^+/Li at various current rates.

3 Results and discussion

3.1 Crystal structure and morphology

First, powder XRD analysis was performed to confirm the purity and crystal structure of pure Co_3O_4, pure $ZnCo_2O_4$ and $ZnCo_2O_4/Co_3O_4$ nanocomposite samples. All thethree samples displayed identical diffraction patterns that could be well indexed to the standard JCPDS data of $ZnCo_2O_4$ (JCPDS no. 01-081-2299) and Co_3O_4 (JCPDS no. 00-043-1003).[28] Since the diffraction peaks of Co_3O_4 are perfectly overlapped with those of $ZnCo_2O_4$ due to their similar structural parameters, it is quite difficult to differentiate them in the nanocomposite sample. More importantly, there were no other impurity peaks observed in XRD patterns, indicating the high purity of the prepared samples. The actual lattice parameters were calculated using Rietveld refinement with the program Fullprof.[29] The Rietveld refinement fit for $ZnCo_2O_4/Co_3O_4$ $ZnCo_2O_4$ and Co_3O_4 in the 2θ range of 20° to 80° using a cubic structure in the $Fd\bar{3}m$ space group is shown in Fig. 1(a)–(c). During the refinement, a pseudo-Voigt function and linear interpolation between a set background point with refinable heights was considered for the profile shape and background, respectively. The lattice parameters obtained from the Rietveld refinement were 8.1309(8), 8.1359(5) and 8.0842(3) Å for $ZnCo_2O_4/Co_3O_4$, $ZnCo_2O_4$ and Co_3O_4, respectively. The lattice parameter of $ZnCo_2O_4$ is slightly larger than that of Co_3O_4 due to presence of Zn ions, which have a slightly larger ionic radius than Co, in the Co site. Further, in the case of $ZnCo_2O_4/Co_3O_4$, there is a minute decrease in the lattice parameter because of the increase in the concentration of Co ions, which have a smaller ionic radius than Zn ions. There is a significant possibility that in the formation of $ZnCo_2O_4/Co_3O_4$ composite, some of Zn sites are occupied by the Co ions and behave like a solid solution. However, very-high-resolution synchrotron data would be required to clearly identify this phenomenon.

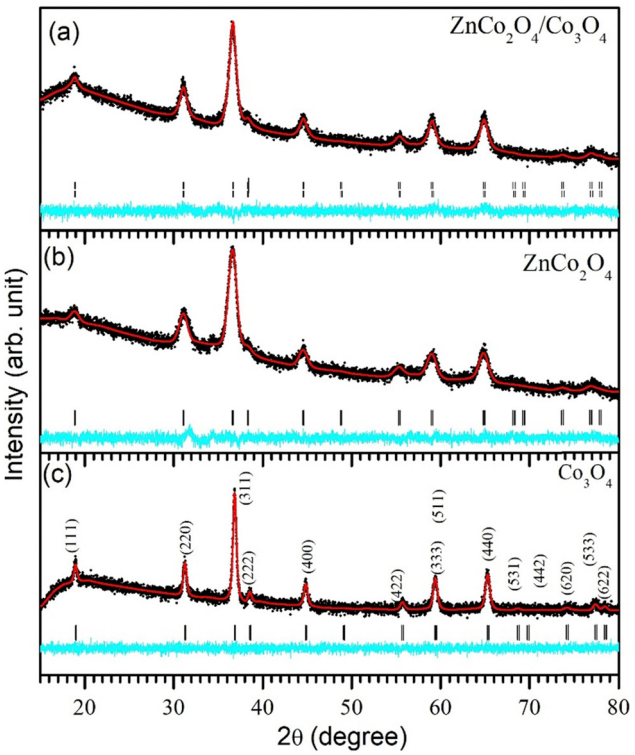

Fig. 1 Rietveld refinement fit on the XRD patterns of (a) $ZnCo_2O_4/Co_3O_4$, (b) $ZnCo_2O_4$ and (c) Co_3O_4 in the 2θ range 20° to 80° using a cubic structure in the $Fd\bar{3}m$ space group. In the figure, black dots, red line and cyan line represent experimental, calculated and difference profiles, respectively, and vertical tick marks above the difference profile show Bragg peak positions.

To further explore the surface morphology of the pure Co_3O_4, pure $ZnCo_2O_4$ and $ZnCo_2O_4/Co_3O_4$ nanocomposite samples, FE-SEM, FE-TEM, HR-TEM and EDS mapping were carried out, and the obtained results are displayed in Fig. 2. Fig. 2(a) shows the nanosheet-like morphology of Co_3O_4, which is actually made up of small-sized interconnected nanoparticles. Numerous voids can easily be seen on the surface of nanosheets, which confirmed the existence of porosity within the sample. Conversely, the FE-SEM images of the pure $ZnCo_2O_4$ (Fig. 2d) and $ZnCo_2O_4/Co_3O_4$ nanocomposite (Fig. 2g) samples clearly showed a 2D ultrathin nanosheet-like morphology. As can be observed, the nanosheets of the pure $ZnCo_2O_4$ sample exhibit rough surfaces with high porosity, which can be attributed to the loss of organic moieties, PVP and gases

 This journal is © the Owner Societies 2024

Published on 05 April 2024. Downloaded on 3/4/2026 1:21:38 AM.

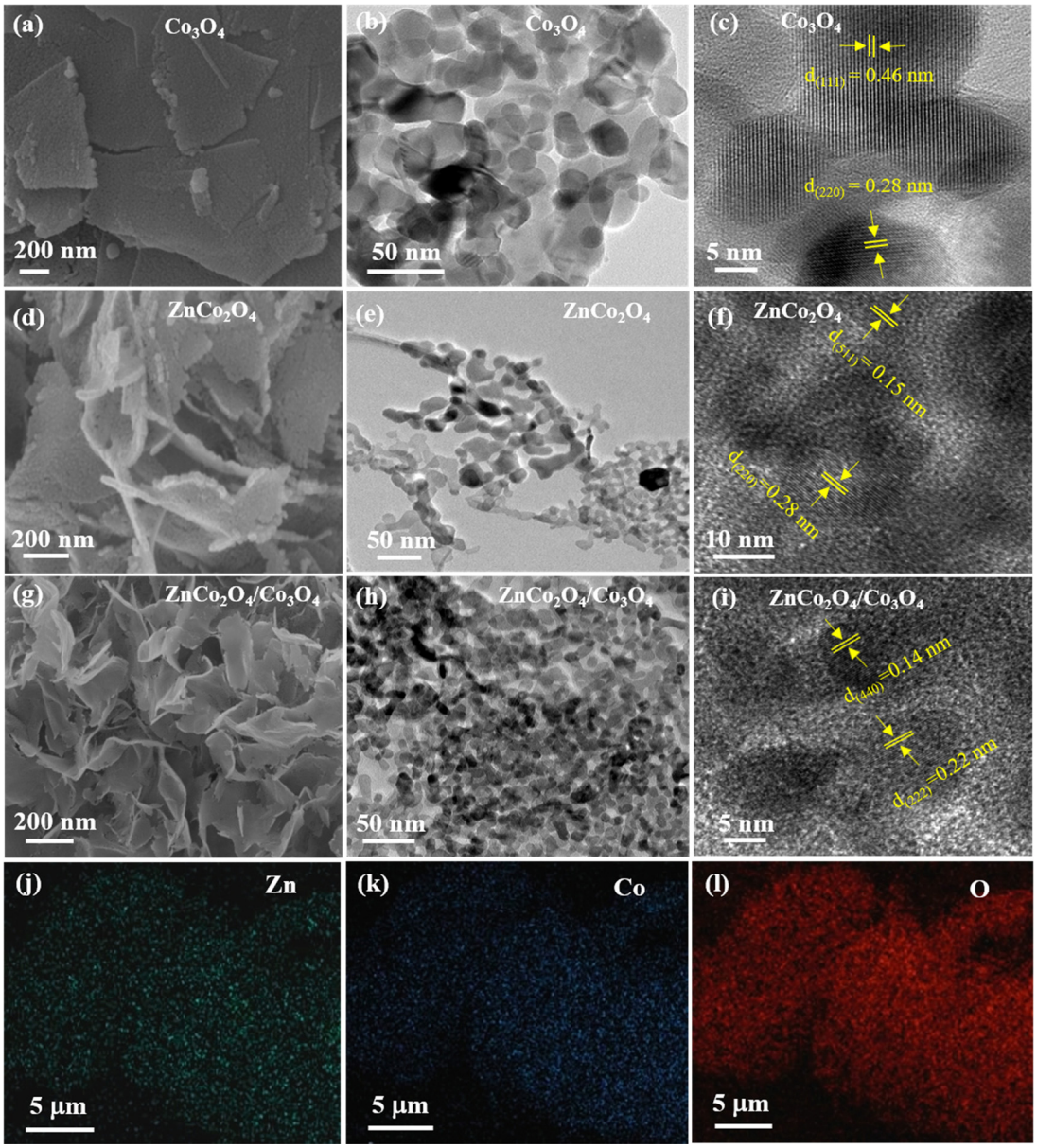

Fig. 2 FE-SEM micrographs (a), (d) and (g), FE-TEM images (b), (e) and (h), and HR-TEM images (c), (f) and (i) of the pure Co_3O_4, pure $ZnCo_2O_4$ and $ZnCo_2O_4/Co_3O_4$ nanocomposite samples, respectively. (j)–(l) Representative energy dispersive X-ray elemental mapping images of the $ZnCo_2O_4/Co_3O_4$ sample.

during the calcination process. However, the $ZnCo_2O_4/Co_3O_4$ nanocomposite sample shows a relatively smooth and intact surface morphology, which may be due to the presence of the additional phase Co_3O_4, promoting better sustainability of the morphology and suppression of the high porosity. Detailed microstructural analysis of all the three samples was further conducted using FE-TEM and HR-TEM analysis. It is evident from Fig. 2(b) that the interconnected nanoparticles have sizes in the range of ~20–35 nm for the Co_3O_4 sample. The white pores between the nanoparticles can be clearly visualized in the FE-TEM image. In contrast, the FE-TEM images of the pure $ZnCo_2O_4$ and $ZnCo_2O_4/Co_3O_4$ nanocomposite samples revealed that both the samples were mainly composed of a large number of small interconnected nodal-shaped nanoparticles with sizes of ~5–40 nm and ~6–15 nm, respectively, as shown in Fig. 2(e) and (h). It can be noticed that the nanocomposite sample has a high density of nanoparticles that are closely interconnected to form a solid network-like structure in comparison to the pure $ZnCo_2O_4$ sample. In contrast, the nanoparticles of the pure $ZnCo_2O_4$ sample are comparatively less intact with poor interconnection and larger pores, resulting in a fragile and broken morphology, as presented in Fig. 2(e). The corresponding HR-TEM images of the pure Co_3O_4, pure $ZnCo_2O_4$ and $ZnCo_2O_4/Co_3O_4$ nanocomposite samples are displayed in Fig. 2(c), (f) and (i), respectively. The HR-TEM image of the Co_3O_4 nanosheet exhibits two lattice fringes of ~0.28 nm and ~0.46 nm

Published on 05 April 2024. Downloaded on 3/4/2026 1:21:38 AM.

corresponding to the (220) and (111) planes of Co_3O_4, respectively, which is in accordance with the XRD result, as shown in Fig. 1(c). Moreover, the interplanar distances were measured to be ~0.15 nm and ~0.28 nm for pure $ZnCo_2O_4$ and ~0.14 nm and ~0.22 nm for the nanocomposite sample, which also matched well with the (511), (220), (440) and (222) planes of the cubic spinel of $ZnCo_2O_4$, respectively. Furthermore, representative energy-dispersive spectroscopy (EDS) of the $ZnCo_2O_4/Co_3O_4$ nanocomposite sample was carried out as shown in Fig. 2(j)–(l), which confirmed the existence of only the elements Zn, Co, and O.

To investigate the specific surface area and pore sizes of the pure Co_3O_4, pure $ZnCo_2O_4$ and $ZnCo_2O_4/Co_3O_4$ nanocomposite samples, BET measurement was performed using N_2 adsorption/desorption isotherms. Fig. 3(a)–(c) clearly show that all the three samples exhibit a typical type-IV isotherm with an H3 hysteresis loop, which demonstrates the existence of mesoporous characteristics in the samples.[15] The BET specific surface areas of the pure Co_3O_4, pure $ZnCo_2O_4$ and $ZnCo_2O_4/Co_3O_4$ nanocomposite samples were found to be ~24.8 $m^2\ g^{-1}$, ~61.4 $m^2\ g^{-1}$ and ~56.7 $m^2\ g^{-1}$, respectively. It is obvious that the pure $ZnCo_2O_4$ sample has a high surface area, which may be due to the existence of numerous pores, as was evident from the FE-SEM and FE-TEM images. The insets of Fig. 3(a)–(c) depict pore size distribution plots generated using Barret–Joyner–Halenda (BJH) analysis. The obtained plots demonstrate a wide distribution of pores in the samples with an average pore diameter of ~15 nm for the pure Co_3O_4 sample, ~9.4 nm for the pure $ZnCo_2O_4$ sample and ~1.4 nm for the $ZnCo_2O_4/Co_3O_4$ nanocomposite sample, which is in agreement with the microstructural analysis. It is believed that the obtained porosity within the samples may provide several surface-active sites, which can allow the passage of electrolytes for better electrode/electrolyte interface and eventually promote fast Li^+ ion insertion/de-insertion reactions in the sample.

A representative XPS analysis was further used to investigate the surface composition and oxidation state of metal ions in the $ZnCo_2O_4/Co_3O_4$ nanocomposite sample, and the obtained results are presented in Fig. 4. The survey spectrum of the sample (Fig. 4a) confirmed the presence of only four elements, *i.e.*, Zn, Co, O and C. The obtained spectra of Zn-2p, Co-2p, and O-1s were fully fitted against a linear-type background using the software XPSPEAK 41. Fig. 4(b) depicts the high resolution spectrum of Zn-2p, which exhibits two prominent peaks located at binding energies of ~1021.4 eV and ~1044.5 eV, corresponding to the spin doublet of Zn $2p_{3/2}$ and Zn $2p_{1/2}$, respectively, indicating the +2 oxidation state of Zn in the nanocomposite sample.[30,31] The high-resolution spectrum of Co-2p shows two spin orbit doublets along with satellite peaks (denoted as Sat.), which mainly belong to Co $2p_{3/2}$ and Co $2p_{1/2}$ components, as shown in Fig. 4(c). The individual components deconvoluted at binding energies of ~779.9 eV and ~794.9 eV confirmed the existence of Co^{3+}, while the obtained binding energies of ~781.3 eV and ~796.5 eV verified the presence of Co^{2+} species.[30–32] Moreover, the high-resolution spectra of O-1s (Fig. 4(d)) displays three peaks at binding energies of ~529.6 eV (O1), ~531.5 eV (O2) and ~532.3 eV (O3), which can be

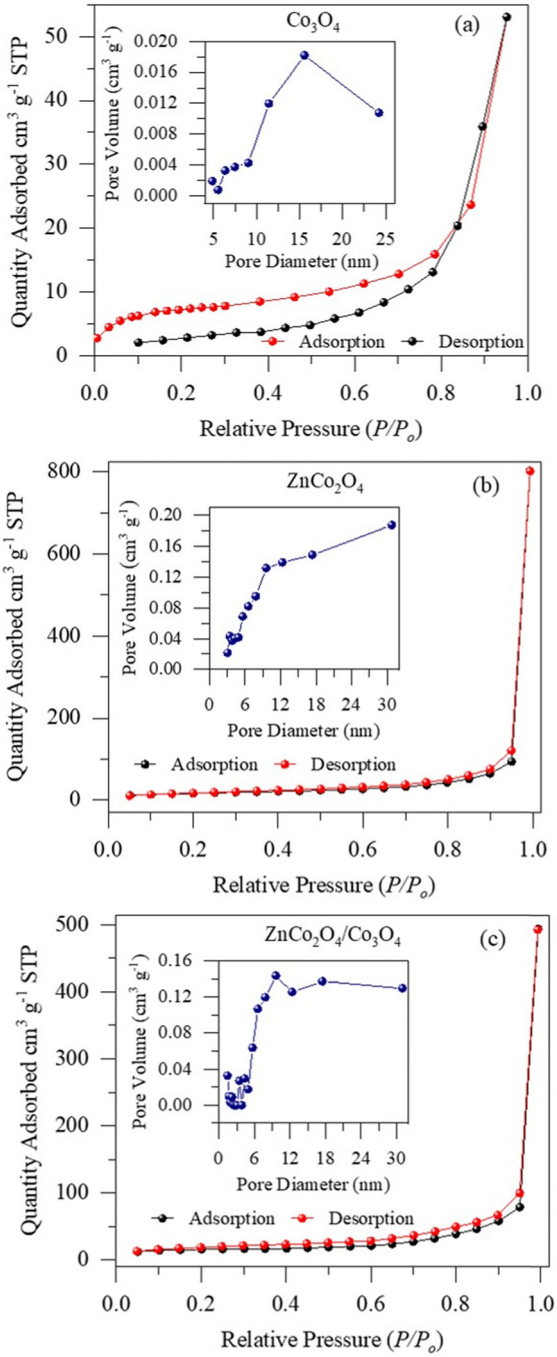

Fig. 3 N_2 adsorption–desorption isotherm with corresponding BJH pore size distribution curve (inset) of the pure Co_3O_4, (a) pure $ZnCo_2O_4$ (b) and $ZnCo_2O_4/Co_3O_4$ nanocomposite (c) samples.

assigned to the metal–oxygen bond and physically/chemically adsorbed water in the surface region. In conclusion, the obtained results confirmed the existence of Zn^{2+}, Co^{3+} and Co^{2+} ions within the $ZnCo_2O_4/Co_3O_4$ nanocomposite sample, which is in agreement with previous literature.[30–32]

3.2 Electrochemical performance

To further analyze the Li^+ ion diffusion mechanism in the pure Co_3O_4, pure $ZnCo_2O_4$ and $ZnCo_2O_4/Co_3O_4$ nanocomposite

 This journal is © the Owner Societies 2024

Published on 05 April 2024. Downloaded on 3/4/2026 1:21:38 AM.

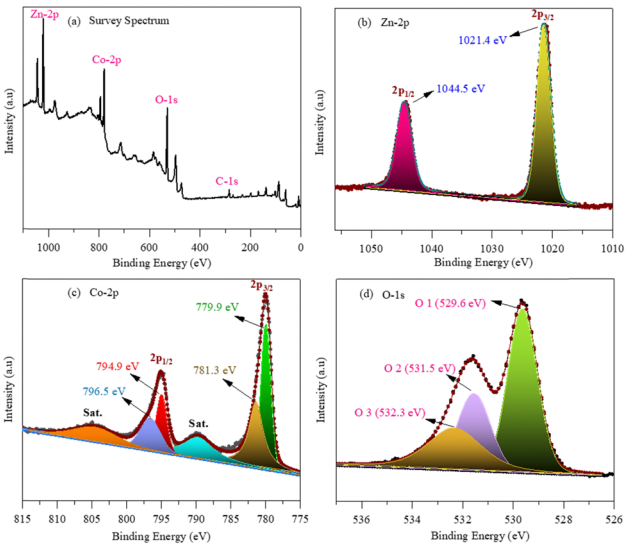

Fig. 4 High resolution XPS spectra of the $ZnCo_2O_4/Co_3O_4$ nanocomposite sample: (a) survey spectrum, (b) Zn-2p, (c) Co-2p and (d) O-1s.

electrodes, cyclic voltammetry (CV) tests were conducted at various scan rates, as depicted in Fig. 5. The reduction peak observed at ~0.96 V during the cathodic sweep of the Co_3O_4 electrode can be ascribed to the multistep electrochemical reduction (lithiation) of Co_3O_4 to metallic cobalt ($Co^{3+} \rightarrow Co^{2+} \rightarrow Co$) embedded in the Li_2O matrix (conversion mechanism), followed by the formation of a solid electrolyte interphase (SEI) film on the electrode surface.[33,34] However, it can be seen that the pure and nanocomposite electrodes exhibit a sharp irreversible cathodic peak at ~0.75 V and ~0.81 V, respectively, at a lower scan rate of 0.1 mV s^{-1}, which can be attributed to the reduction of $ZnCo_2O_4$ to Zn^0 and Co^0, followed by SEI layer formation on electrode surfaces. Additionally, a weak peak appeared at ~0.41 V for the pure $ZnCo_2O_4$ and ~0.38 V for the $ZnCo_2O_4/Co_3O_4$ nanocomposite electrode, which is in fact due to the further lithiation of Zn^0 to form a Li–Zn alloy, as described in eqn (iii).[30,35–37] However, the cathodic peaks became wide during the subsequent scanning and shifted to ~0.86 V and ~0.95 V for the pure $ZnCo_2O_4$ and $ZnCo_2O_4/Co_3O_4$ nanocomposite electrodes, respectively, which corresponds to the reduction of ZnO to metallic Zn and Co_3O_4/CoO to metallic Co.[30,36] The notable disparity between the first and subsequent scans indicates a change in lithium-ion insertion reactions. On the contrary, two oxidation peaks were observed at ~1.6 V and ~2.1 V during the anodic sweep for all three electrodes, which are due to the reversible oxidation (de-lithiation) of the metallic Co to Co^{2+}/Co^{3+} of the Co_3O_4 and Zn of $ZnCo_2O_4$ to Zn^{2+} and Co^{3+}, respectively, along with the decomposition of the SEI film (eqn (iv)–(vi)).[38,39] The binary

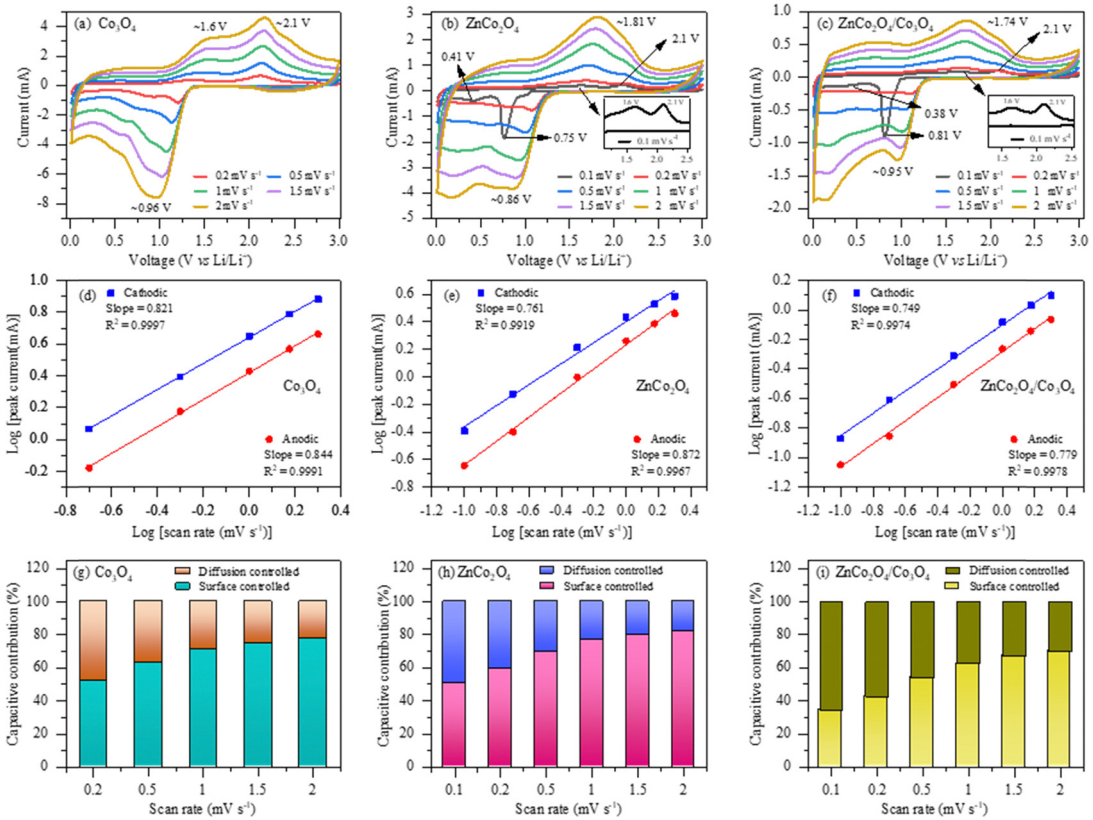

Fig. 5 (a)–(c) Cyclic voltammetry curves at various scan rates; (d)–(f) linear relationship between the logarithm of peak current and scan rates; and (g)–(i) corresponding capacitive and diffusion contribution ratios at different scan rates for the pure Co_3O_4, pure $ZnCo_2O_4$ and $ZnCo_2O_4/Co_3O_4$ nanocomposite electrodes, respectively.

Published on 05 April 2024. Downloaded on 3/4/2026 1:21:38 AM.

metal oxide Co_3O_4 generally shows a normal spinel structure in which the Co^{3+} and Co^{2+} ions are octahedrally and tetrahedrally coordinated in a cubic close-packed oxide anion lattice, respectively, which demonstrates multistep redox reactions of $Co^{3+}/Co^{2+}/Co$ during the lithiation/de-lithiation process.[11] As can be seen, the oxidation peaks of the pure $ZnCo_2O_4$ and $ZnCo_2O_4/Co_3O_4$ nanocomposite electrodes shifted to ~1.81 V and ~1.74 V during subsequent anodic scans, respectively. At various subsequent scan rates ranging from 0.2 to 2 mV s^{-1}, all CV curves exhibit a similar shape with nominal shift of reduction and oxidation peaks, indicating high reversibility with small polarization.[40,41]

According to previous reports,[30,36,39] the electrochemical reaction mechanism involved in the active materials of Co_3O_4 and $ZnCo_2O_4$ during the Li^+ ion insertion and de-insertion processes can be summarized as follows:

$$Co_3O_4 + 8Li^+ + 8e^- \rightarrow 4Li_2O + 3Co^0 \quad \text{(i)}$$

$$ZnCo_2O_4 + 8Li^+ + 8e^- \rightarrow Zn + 2Co + 4Li_2O \quad \text{(ii)}$$

$$Zn + Li^+ + e^- \rightarrow LiZn \quad \text{(iii)}$$

$$Zn + Li_2O \leftrightarrow ZnO + 2Li^+ + 2e^- \quad \text{(iv)}$$

$$Co + Li_2O \leftrightarrow CoO + 2Li^+ + 2e^- \quad \text{(v)}$$

$$3CoO + Li_2O \leftrightarrow Co_3O_4 + 2Li^+ + 2e^- \quad \text{(vi)}$$

Moreover, the kinetic behavior of lithium storage in all three electrodes can be examined by applying the power law, which is a widely applied approach to determine the storage mechanism to be either a surface-induced capacitance process or diffusion-controlled insertion process.[42,43] Typically, the relationship between the measured peak current (i) and scan rate (v) can be expressed using eqn (vii) and (viii).

$$i = av^b \quad \text{(vii)}$$

$$\log(i) = \log(a) + b\log(v) \quad \text{(viii)}$$

Here, 'a' and 'b' refer to adjustable empirical constants.[44,45] The 'b' values can be obtained from the slope of the linear relationship between $\log(i)$ and $\log(v)$, as shown in Fig. 5(d)–(f). The 'b' values range between 0.5 and 1; it has been reported that the diffusion-controlled process is significant if the 'b' value is close to or equal to 0.5. However, if the 'b' values are close to or equal to 1, the electrode will exhibit ideal surface-induced capacitive behavior.[45,46] The 'b' values were calculated after plotting the graph between $\log(i)$ *versus* $\log(v)$ for all the three electrodes during anodic and cathodic processes and were calculated to be ~0.844 and ~0.821 for the pure Co_3O_4 electrodes, ~0.761 and ~0.872 for the pure $ZnCo_2O_4$ electrodes and ~0.749 and ~0.779 for the $ZnCo_2O_4/Co_3O_4$ nanocomposite electrodes, suggesting that the surface-induced capacitive behavior is dominant in the Li^+ ion diffusion mechanism. Thereafter, the contribution ratios of diffusion-controlled and surface-controlled capacitive mechanisms were quantified using following equations:[45,47]

$$i(V) = k_1v + k_2v^{1/2} \quad \text{(ix)}$$

$$i(V)/v^{1/2} = k_1v^{1/2} + k_2, \quad \text{(x)}$$

where v and $i(V)$ represent the scan rate and total current at constant potential, respectively, while k_1v and $k_2v^{1/2}$ stand for surface-controlled capacitive behavior and diffusion-controlled contributions, respectively. Furthermore, eqn (x), which is a simple rearrangement of eqn (ix), was used to calculate the values of constants k_1 and k_2. These constants were utilized to determine the slope and intercept of the linear fitting of the plot of $i(V)/v^{1/2}$ *vs.* $v^{1/2}$ at a constant potential. The percentage contribution ratio of the surface-controlled capacitive and diffusion-controlled mechanisms at various scan rates of all the three electrodes are summarized in Fig. 5(g)–(i). It can be noticed that the surface-controlled capacitive contribution increases with increasing scan rate, which indicates that the electrode surfaces are highly active for Li^+ ion storage at high scan rates. More importantly, the surface-controlled capacitive mechanism is higher for the pure $ZnCo_2O_4$ electrode than the nanocomposite electrode.

Fig. 6(a)–(c) depicts the galvanostatic discharge/charge profiles of the pure Co_3O_4, pure $ZnCo_2O_4$ and $ZnCo_2O_4/Co_3O_4$ nanocomposite electrodes for the 1st, 2nd, 50th and 100th cycles at 0.5C within the potential range of 0.01–3.0 V (*vs.* Li/Li^+). During the first discharge of the Co_3O_4 electrode, two voltage plateaus at ~1.2 V and ~1.1 V are clearly seen, followed by a gradual sloping region until the cutoff voltage of ~0.01 V, which can be ascribed to the reduction of Co_3O_4 to metallic cobalt and formation of the SEI film, respectively.[44] The other two $ZnCo_2O_4$ and $ZnCo_2O_4/Co_3O_4$ nanocomposite electrodes exhibit a short and long voltage plateau at ~0.6 V and ~0.9 V during the 1st discharge and later gradually decline until the cut-off potential of ~0.01 V, which is obviously due to the reduction of $ZnCo_2O_4$ to Zn and Co followed by the formation of the Li–Zn alloy.[48] The obtained discharge/charge voltage plateaus of the electrodes matched well with redox peaks observed in CV results. The initial discharge/charge capacities of the pure Co_3O_4, $ZnCo_2O_4$ and $ZnCo_2O_4/Co_3O_4$ nanocomposite electrodes were found to be 1233.4/938.8 mA h g^{-1}, 1529/989 mA h g^{-1} and 1020/681 mA h g^{-1} with Coulombic efficiencies of 76%, 64% and 66%, respectively. The significant capacity loss in the first charge cycle can be attributed to the formation of the SEI layer caused by the electrolyte degradation, which prevents the complete de-insertion of Li^+ ions from the active materials, resulting in the irreversible capacity loss. From the 2nd cycle onwards, the discharge/charge capacities of the pure Co_3O_4 electrode started to increase and reached 1001.8/954.6 mA h g^{-1} for the 2nd cycle and 1509.6/1474.5 mA h g^{-1} for the 100th cycle with a Coulombic efficiency of 95.2% and 97.6%, respectively, which may be due to the continuous activation of the electrode because of the large surface area and high porosity. However, the discharge/charge capacity of the pure $ZnCo_2O_4$ electrode decreased in the 2nd, 50th and 100th cycles. In contrast, the capacity of the nanocomposite electrode significantly increased after the 1st cycle and reached a capacity of 1010/1024 mA h g^{-1} at the 100th cycle, which is not only greater than the capacity of the pure $ZnCo_2O_4$

 This journal is © the Owner Societies 2024

Published on 05 April 2024. Downloaded on 3/4/2026 1:21:38 AM.

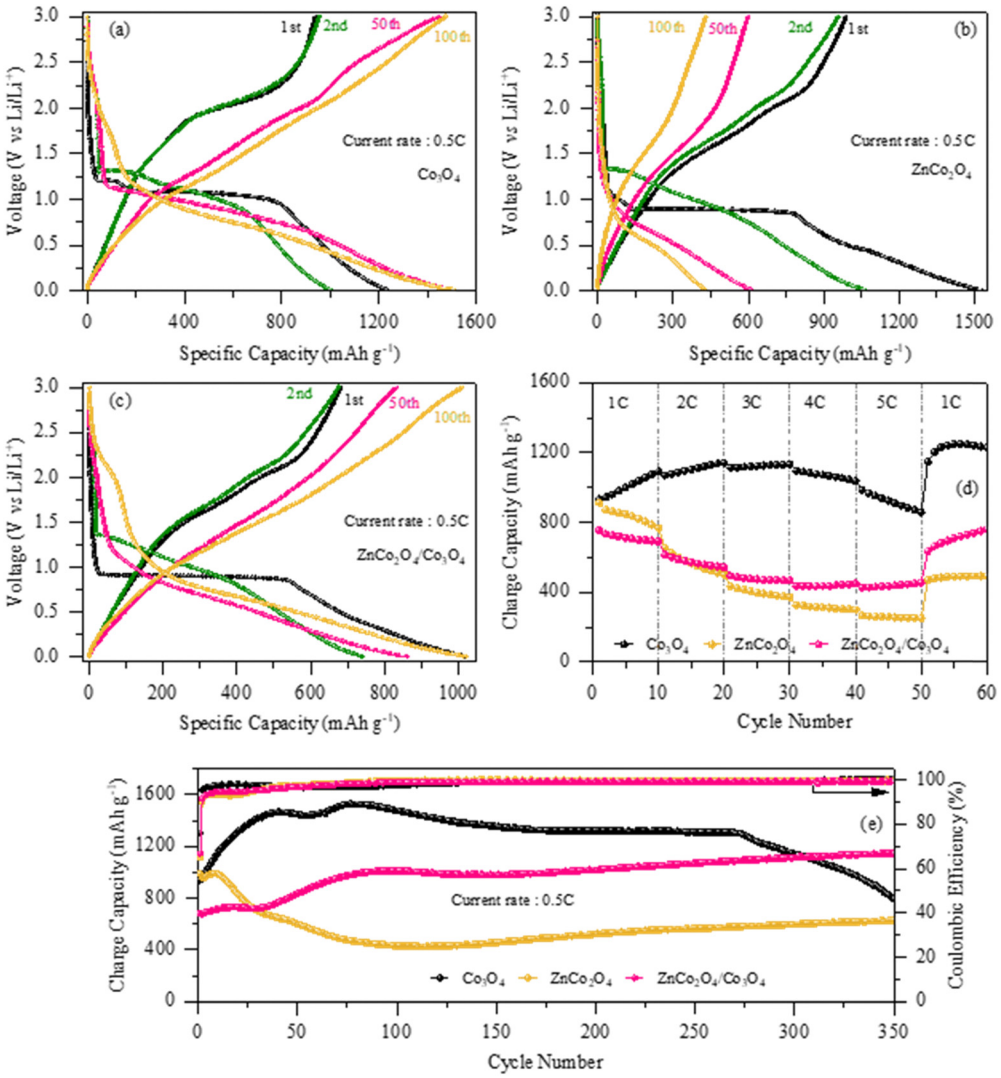

Fig. 6 (a)–(c) Charge/discharge profiles at 0.5C; (d) rate performance at various C-rates; and (e) cycling performances at 0.5C over 350 cycles of the pure Co_3O_4, pure $ZnCo_2O_4$ and $ZnCo_2O_4/Co_3O_4$ nanocomposite electrodes, respectively.

electrode (431/429 mA h g^{-1} at the 100th cycle) but also higher than the theoretical capacity of $ZnCo_2O_4$ (~903 mA h g^{-1}). Although the $ZnCo_2O_4/Co_3O_4$ nanocomposite electrode shows high capacity with better electrochemical reversibility (100% Coulombic efficiency) than pure $ZnCo_2O_4$, it is believed that the synergistic effect between $ZnCo_2O_4$ and Co_3O_4 offers more active sites for lithium ion storage.

Fig. 6(d) presents a comparative analysis of the rate performances of the pure Co_3O_4, $ZnCo_2O_4$ and $ZnCo_2O_4/Co_3O_4$ nanocomposite electrodes at various C-rates. From the overall profile, it can be observed that Co_3O_4 shows excellent performance at all current rates with specific capacities of 1116.5, 1164.2, 1158.7, 1069.1 and 889.7 mA h g^{-1} at 1C, 2C, 3C, 4C and 5C, respectively, which are much higher than the capacities of the $ZnCo_2O_4/Co_3O_4$ nanocomposite electrode (691 mA h g^{-1}, 543 mA h g^{-1}, 468 mA h g^{-1}, 449 mA h g^{-1} and 454 mA h g^{-1}) and pure $ZnCo_2O_4$ electrode (767 mA h g^{-1}, 499 mA h g^{-1}, 372 mA h g^{-1}, 299 mA h g^{-1} and 250 mA h g^{-1}) at same current rates. More importantly, it should be noted that the obtained capacity of the Co_3O_4 electrode, especially at the high current rate of 5C, is almost same to the theoretical capacity of the Co_3O_4 electrode (~890 mA h g^{-1}), which clearly demonstrates the promising potential characteristics of the Co_3O_4 anode. Additionally, when the current rate was reverted to the initial rate of 1C, the charge capacities of the pure Co_3O_4 electrode and $ZnCo_2O_4/Co_3O_4$ nanocomposite electrode remained considerably higher after 60 cycles (1229.3 mA h g^{-1} and 759.8 mA h g^{-1}, respectively) than that of the pure $ZnCo_2O_4$ electrode (493.7 mA h g^{-1}), which may be due to the higher structural stability and reduced charge transfer resistance within these two electrodes. It can be seen that the capacity started to decrease with increasing current rates in all the electrodes, which is generally due to the slow diffusion rate of Li^+ ions into the electrode material at high current rates.

To further examine the long-term cycle life of all the three electrodes, cyclability tests were performed at 0.5C for 350 cycles,

Published on 05 April 2024. Downloaded on 3/4/2026 1:21:38 AM.

and the obtained results are presented in Fig. 6(e). At first sight, it can be seen that the charge capacity of the pure Co_3O_4 electrode significantly increased to 1462.8 mA h g^{-1} during the first 40 cycles, which can be attributed to the formation/decomposition of a reversible polymeric gel-like film on the electrode surface due to electrolyte degradation.[49,50] Thereafter, the charge capacity was found to decrease slightly from the 40th to 60th cycle, at which the capacity was 1447.7 mA h g^{-1}, which may be due to the restriction of Li^+ ion extraction during charging due to the formation of an unstable SEI film, indicating that the conversion reaction may not be fully reversible after a certain cycle number, and therefore, capacity loss is observed in the successive cycles. Furthermore, the Co_3O_4 electrode exhibits a slow drop in capacity up to 270 cycles, at which it retained a charge capacity of 1304.1 mA h g^{-1} with a Coulombic efficiency of nearly 100%. Then, the charge capacity rapidly begins to decline, and retained a maximum capacity of only 794.7 mA h g^{-1} after 350 cycles, which clearly indicates that the obtained morphology of the porous nanosheet-like Co_3O_4 could not be withstand being used as an anode during long-term cycling. It is believed that the porous nanosheet-like structure of the Co_3O_4 anode, which is mainly composed of small-sized interconnected nanoparticles with numerous pores, becomes pulverized during long-range cycling due to the repeated volume expansion/contraction during charge and discharge. Unfortunately, the obtained decreasing trend of the Co_3O_4 anode clearly indicates that the capacity will reach zero in further consecutive cycles. More importantly, the obtained zig-zag trend is common and usually occurs in transition-metal-oxide anode materials for LIBs.[51–53] Similarly, the charge capacity of the pure $ZnCo_2O_4$ electrode drops quickly over the first 114 cycles with a capacity retention of only ~424 mA h g^{-1}. Thereafter, the capacity began to increase and a charge capacity of 628.8 mA h g^{-1} was observed after 350 cycles with a Coulombic efficiency of 100%. Conversely, the $ZnCo_2O_4$/Co_3O_4 nanocomposite electrode exhibits a significant stepwise increase in the capacity as the cycle number increases and demonstrates a charge capacity of 1011 mA h g^{-1} after 100 cycles with 100% Coulombic efficiency. After 125 cycles, it can be noted that the charge capacity of the nanocomposite electrode is improved, and it retained a capacity of 1146.2 mA h g^{-1} after 350 cycles, which is nearly double of the capacity of pure electrode. Since the capacity of the nanocomposite electrode is remarkably higher than that of the pure Co_3O_4 and $ZnCo_2O_4$ electrodes, it is believed that the sustainable morphology with optimum porosity as well as the strong synergistic effect between the two electrochemically active materials, *i.e.*, $ZnCo_2O_4$ and Co_3O_4, offered not only more active sites for Li^+ ion diffusion but also effectively buffered the dramatic volume change and maintained the mechanical integrity during Li^+ ion insertion/extraction. However, in the case of the pure $ZnCo_2O_4$ electrode, the high porosity and weak connectivity between the nanoparticles lead to fast capacity fading and poor structural stability during prolonged cycling. In addition, it is reasonable to suggest that the additional phase Co_3O_4 may provide superior surface stability and high structural stability to prevent the detachment of the $ZnCo_2O_4$ active materials during lithiation/de-lithiation processes. At the same time, Co_3O_4 may also accelerate the electrochemical reactions by effectively storing eight lithium ions per formula unit due to its high electrochemical activity (Co_3O_4 + $8Li^+ + 8e^- \leftrightarrow 3Co + 4Li_2O$) and contribute to the total capacity of the host material.

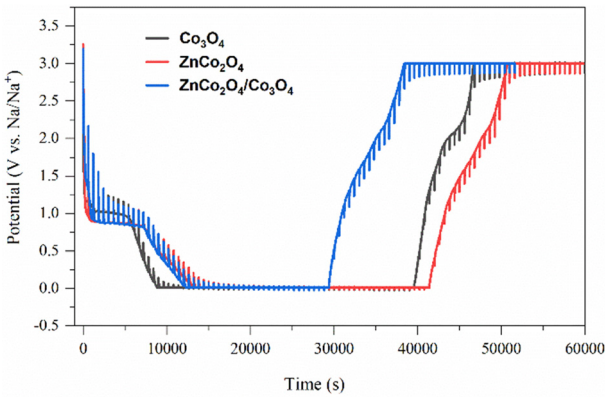

Fig. 7 GITT analysis of the pure Co_3O_4, $ZnCo_2O_4$, and $ZnCo_2O_4$/Co_3O_4 nanocomposite electrodes.

Fig. 7 shows the galvanostatic intermittent titration technique (GITT) analysis, which exhibits the lithium-ion diffusion kinetics of the electrode materials (Co_3O_4, $ZnCo_2O_4$, and $ZnCo_2O_4$/Co_3O_4) during discharge and charge processes. All the three electrodes were discharged and charged at a C-rate of 0.5C for 10 minutes, then left open for 30 minutes in the voltage range of 0.01–3.0 V for GITT analysis. The GITT investigation consists of a sequence of current pulses followed by relaxation periods, in which no current flows through the cell. During the positive current pulse, the cell potential rapidly increases to a level proportional to the *iR* drop. Thereafter, the potential gradually increases due to the galvanostatic charge pulse, which maintains a constant concentration gradient. When the current pulse is interrupted during the relaxation period, the composition in the electrode tends to become homogeneous due to Li^+ diffusion, resulting in the sudden drop in the potential to a level proportional to the *iR* drop, followed by a gradual decrease until equilibrium is achieved. During a negative current pulse, the opposite sequence occurs. The cell potential quickly decreases to a level proportional to the *iR* drop, followed by a slow decrease during the galvanostatic discharge pulse. During the relaxation period, the potential experiences a sudden increase proportional to the *iR* drop, followed by a gradual rise until equilibrium is attained. As can be seen from the GITT profiles of all the three electrodes, the time required for discharge/charge processes is less for the $ZnCo_2O_4$/Co_3O_4 nanocomposite electrode than the other two, which clearly indicates high Li^+ diffusion kinetics for this sample as well justifying the obtained high electrochemical performances of the nanocomposite electrode.

The electrochemical behavior of all the three electrodes was further investigated through electrochemical impedance spectroscopy (EIS) analysis, as depicted in Fig. 8. The Nyquist plot of each electrode consists of a depressed semicircle in the high-frequency region and a sloping line in the low-frequency

 This journal is © the Owner Societies 2024

Published on 05 April 2024. Downloaded on 3/4/2026 1:21:38 AM.

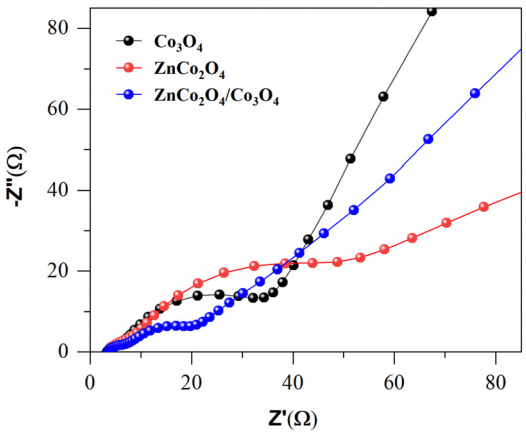

Fig. 8 EIS analysis of the pure Co_3O_4, $ZnCo_2O_4$, and $ZnCo_2O_4/Co_3O_4$ nanocomposite electrodes.

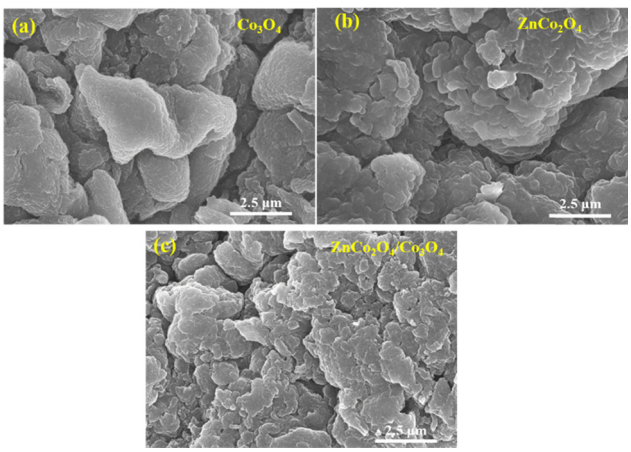

Fig. 9 *Ex situ* SEM images of the (a) pure Co_3O_4, (b) pure $ZnCo_2O_4$ and (c) $ZnCo_2O_4/Co_3O_4$ nanocomposite electrodes after 350 cycles.

region. The semicircle observed in the high frequency range signifies the charge transfer resistance (R_{CT}) at the electrode/electrolyte interface, while the inclined line in the low-frequency region represents the Warburg impedance, reflecting electrolyte diffusion within the electrode. A smaller diameter of the semicircle indicates lower R_{CT} and higher Li^+ diffusion kinetics. The observed EIS spectrum demonstrates that the $ZnCo_2O_4/Co_3O_4$ nanocomposite electrode exhibits the lowest R_{CT} compared to the pure $ZnCo_2O_4$ and pristine Co_3O_4 electrodes. These results are in good accordance with the cycling performance data of all the electrodes.

To explain long-term cycling performances, *ex situ* SEM images of the pure Co_3O_4, $ZnCo_2O_4$, and $ZnCo_2O_4/Co_3O_4$ nanocomposite electrodes were taken after 350 cycles, and the results are displayed in Fig. 9. It is clearly evident that the $ZnCo_2O_4/Co_3O_4$ nanocomposite electrode retains its structural integrity to a certain extent during long-range cycling compared to the other two electrodes, which further verifies the enhanced electrochemical performance of the nanocomposite electrode.

Since numerous reports have been published on the different nanostructures and composites of $ZnCo_2O_4$, a comprehensive table has been compiled to facilitate a clear comparison between previous and current studies. As can be seen from Table 1, the current 2D ultrathin nanosheet-like $ZnCo_2O_4/Co_3O_4$ nanocomposite electrode delivered superior electrochemical performance among all reported $ZnCo_2O_4$ data.

4 Conclusions

In summary, we have successfully synthesized a $ZnCo_2O_4/Co_3O_4$ nanocomposite sample using a facile hydrothermal approach, which is comprised of a large number of small interconnected nodal-shaped nanoparticles. To obtain the additional phase Co_3O_4, a nonstoichiometric ratio between Zn and Co was simply maintained. To accommodate two electrochemically active anode materials in one frame rather than one anode was the motive behind introducing the additional phase Co_3O_4 along with $ZnCo_2O_4$ in this work. With the introduction of Co_3O_4, the $ZnCo_2O_4/Co_3O_4$ nanocomposite sample exhibits visibly enhanced electrochemical properties compared to the pure $ZnCo_2O_4$ and pure Co_3O_4 samples. It is believed that the additional phase Co_3O_4 provides a smooth and intact surface morphology, which helps in alleviating the mechanical stress induced by the Li^+ insertion/extraction process and preserves the integrity of the nanocomposite morphology. Furthermore,

Table 1 Comparison of the electrochemical performances of the current 2D ultrathin nanosheet-like $ZnCo_2O_4/Co_3O_4$ electrode with those of previously reported $ZnCo_2O_4$ electrodes based on various morphologies/composites

Material	Morphology	Specific capacity/cycle no./current density/rate	Ref.
$ZnCo_2O_4$	Nanoparticle	801 mA h g^{-1}/100/100 mA g^{-1}	54
$ZnCo_2O_4$	Nanorods	767.15 mA h g^{-1}/50/0.2 mA cm^{-2}	55
$ZnCo_2O_4$	Flower-like	940 mA h g^{-1}/100/0.1C	56
$ZnCo_2O_4$	Sliced orange-shaped	890 mA h g^{-1}/130/200 mA g^{-1}	57
$ZnCo_2O_4$	Nanoparticle	900 mA h g^{-1}/60/60 mA g^{-1}	58
$ZnCo_2O_4$	Nano-structured Spinel	1000 mA h g^{-1}/120/0.5C	59
$ZnCo_2O_4$	3D Plum like	746 mA h g^{-1}/110/500 mA g^{-1}	60
$ZnCo_2O_4$	Pineapple shaped	1132 mA h g^{-1}/120/100 mA g^{-1}	61
$ZnCo_2O_4$/Graphene	Nanoparticle	299.8 mA h g^{-1}/70/0.1C	62
$ZnCo_2O_4$/Graphene	Sheet-like	791 mA h g^{-1}/1000/1 A g^{-1}	63
Co_3O_4@$ZnCo_2O_4$@NC	Porous nanowires	931 mA h g^{-1}/50/100 mA g^{-1}	64
$ZnCo_2O_4/Co_3O_4$	2D ultrathin nanosheet-like	1146.2 mA h g^{-1}/350/0.5C	This work

Published on 05 April 2024. Downloaded on 3/4/2026 1:21:38 AM.

Co_3O_4 may participate in the electrochemical reactions due to its highly electrochemical active nature and thereby enhance the electrochemical performance of the $ZnCo_2O_4$ anode. Based on these structural features and the synergistic effect between $ZnCo_2O_4$ and Co_3O_4, the nanocomposite electrode exhibits superior performance with long-term cycling stability, such as a charge capacity of 1146.2 mA h g^{-1} at 0.5C after 350 cycles. Hence, it can be concluded that the $ZnCo_2O_4/Co_3O_4$ nanocomposite holds significant potential as an anode material for LIBs.

Conflicts of interest

There are no conflicts to declare.

Acknowledgements

Anubha Tomar would like to express her sincere gratitude to CSIR, New Delhi, India for the award of senior research fellowship (09/045(1687)/2019-EMR-1). Dr Alok Kumar Rai is grateful to University Grants Commission (UGC) for the position under UGC-FRP scheme (FRP ID: 57304). This work was mainly supported by the Faculty Research Programme Grant (Ref. No./IoE/2023-24/12/FRP), sanctioned by Institution of Eminence, University of Delhi and partially supported by the National Research Foundation of Korea (NRF) through a grant funded by the Korea government (MSIT) (NRF-2018R1A5A1025224).

References

1 A. Pan, Y. Wang, W. Xu, Z. Nie, S. Liang, Z. Nie, C. Wang, G. Cao and J. G. Zhang, *J. Power Sources*, 2014, **255**, 125–129.
2 Y. Tan, C. Yang, W. Qian, X. Sui, C. Teng, Q. Li and Z. Lu, *J. Alloys Compd.*, 2021, **855**, 157387.
3 L. Zhang, B. R. Lu, F. H. Cao, Z. L. Yu, H. P. Cong and S. H. Yu, *J. Mater. Chem. A*, 2018, **6**, 12962–12968.
4 L. Kong, L. Wang, D. Sun, S. Meng, D. Xu, Z. He, X. Dong, Y. Li and Y. Ji, *Molecules*, 2019, **24**, 3149.
5 Z. Li, B. Li, L. Yin and Y. Qi, *ACS Appl. Mater. Interfaces*, 2014, **6**, 8098–8107.
6 H. Xiao, Y. Li, R. Chen, T. Xie, P. Xu, H. Zhu, J. He, W. Zheng and S. Huang, *eScience*, 2023, **3**, 100134.
7 Z. Song, H. Liu, B. Chen, Q. Jiang, F. Sui, K. Wu, Y. Cheng and B. Xiao, *Phys. Chem. Chem. Phys.*, 2024, **26**, 1406–1427.
8 Y. Fang, D. Luan and X. W. Lou, *Adv. Mater.*, 2020, **32**, 2002976.
9 Y. Fang, D. Luan, Y. Chen, S. Gao and X. W. Lou, *Angew. Chem., Int. Ed.*, 2020, **59**, 2644.
10 Y. Fang, B. Y. Guan, D. Luan and X. W. Lou, *Angew. Chem., Int. Ed.*, 2019, **58**, 7739.
11 H. S. Jadhav, A. K. Rai, J. Y. Lee, J. Kim and C. J. Park, *Electrochim. Acta*, 2014, **146**, 270–277.
12 S. Abouali, M. A. Garakani, B. Zhang, H. Luo, Z. L. Xu, J. Q. Huang, J. Huang and J. K. Kim, *J. Mater. Chem. A*, 2014, **2**, 16939–16944.
13 H. Du, K. Huang, M. Li, Y. Xia, Y. Sun, M. Yu and B. Geng, *Nano Res.*, 2018, **11**, 1490–1499.
14 J. Wang, H. Wang, F. Li, S. Xie, G. Xu, Y. She, M. K. H. Leung and T. Liu, *J. Mater. Chem. A*, 2019, **7**, 3024–3030.
15 S. Baji, S. V. Nair and A. K. Rai, *J Solid State Electr.*, 2017, **21**, 2869–2875.
16 G. Zhang and X. W. Lou, *Angew. Chem.*, 2014, **126**, 9187–9190.
17 M. Chen, X. Xia, J. Yin and Q. Chen, *Electrochim. Acta*, 2015, **160**, 15–21.
18 J. S. Chen, T. Zhu, Q. H. Hu, J. Gao, F. Su, S. Z. Qiao and X. W. Lou, *ACS Appl. Mater. Interfaces*, 2010, **2**, 3628–3635.
19 X. Yao, X. Xin, Y. Zhang, J. Wang, Z. Liu and X. Xu, *J. Alloys Compd.*, 2012, **521**, 95–100.
20 Y. Ding, P. Zhang, Z. Long, Y. Jiang, J. Huang, W. Yan and G. Liu, *Mater. Lett.*, 2008, **62**, 3410–3412.
21 A. Tomar, E. Adhitama, M. Winter, T. Placke and A. K. Rai, *Batteries Supercaps*, 2023, **6**, e202200465.
22 J. Singh, S. Lee, P. Yadav, S. Kim, J. Kim and A. K. Rai, *ACS Appl. Energy Mater.*, 2022, **5**, 126–136.
23 A. K. Rai, T. V. Thi, B. J. Paul and J. Kim, *Electrochim. Acta*, 2014, **146**, 577–584.
24 L. Yu, G. Zhang, C. Yuan and X. W. Lou, *Chem. Commun.*, 2013, **49**, 137–139.
25 G. Zhang, B. Y. Xia, C. Xiao, L. Yu, X. Wang, Y. Xie and X. W. Lou, *Angew. Chem.*, 2013, **125**, 8805–8809.
26 G. Zhang, L. Yu, H. B. Wu, H. E. Hoster and X. W. Lou, *Adv. Mater.*, 2012, **24**, 4609–4613.
27 J. Liu, Q. Xia, Y. Wang and H. Xia, *Mater. Lett.*, 2017, **193**, 220–223.
28 H. Li, L. Wang, Y. Guan, Y. Su, J. Mu, H. Che, A. Liu and Z. Guo, *Appl. Phys. A: Mater. Sci. Process.*, 2018, **124**, 1–10.
29 J. Rodriguez-Carvajal, *FullProf; Laboratoire Leon Brillouin, CEA-CNRS CEA/Saclay:91191*, Gif sur Yvette Cedex, France, 2008.
30 H. Xu, Y. Zhang, X. Song, X. Kong, T. Ma and H. Wang, *J. Alloys Compd.*, 2020, **821**, 153289.
31 M. Carbone, *J. Electroanal. Chem.*, 2018, **815**, 151e157.
32 S. Cheng, Q. Ru, P. Liu, H. Yan, Z. Shi, X. Hou, S. Su, L. Zhao and F. C. C. Ling, *J. Alloys Compd.*, 2019, **809**, 151703.
33 J. Qiu, M. Yu, Z. Zhang, X. Cai and G. Guo, *J. Alloys Compd.*, 2019, **775**, 366–371.
34 Y. Jiang, X. Yan, P. Mei, Y. Zhang, W. Xiao and H. Tang, *J. Alloys Compd.*, 2018, **764**, 80–87.
35 Z. Zhao, G. Tian, V. Trouillet, L. Zhu, J. Zhu, A. Missiul, E. Welter and S. Dsoke, *Inorg. Chem. Front.*, 2019, **6**, 1861–1872.
36 X. Song, Q. Ru, Y. Mo, S. Hu and B. An, *J. Alloys Compd.*, 2014, **606**, 219–225.
37 M. Du, D. He, Y. Lou and J. Chen, *J. Energy Chem.*, 2017, **26**, 673–680.
38 Y. Jiang, X. Yan, P. Mei, Y. Zhang, W. Xiao and H. Tang, *J. Alloys Compd.*, 2018, **764**, 80–87.
39 Z. Wang, Q. Ru, X. Chen, Q. Guo, B. Wang, X. Hou and S. Hu, *ChemElectroChem*, 2017, **4**, 2218–2224.
40 P. Gurunathan, P. M. Ette, N. Lakshminarasimhan and K. Ramesha, *ACS Omega*, 2017, **2**, 7647–7657.

 This journal is © the Owner Societies 2024

Published on 05 April 2024. Downloaded on 3/4/2026 1:21:38 AM.

41 M. Zhong, W. W. He, W. Shuang, Y. Y. Liu, T. L. Hu and X. H. Bu, *Inorg. Chem.*, 2018, **57**, 4620–4628.
42 W. Bai, H. Tang, J. Zhai, C. Cui, W. Wang, C. Cheng, E. Ren, H. Xiao, M. Zhou, R. Guo and S. Lin, *Ind. Eng. Chem. Res.*, 2022, **61**, 12555–12566.
43 J. Deng, X. Yu, Y. He, B. Li, Q. H. Yang and F. Kang, *Energy Storage Mater.*, 2017, **6**, 61–69.
44 Y. H. Lu, J. H. Li, Z. F. Xu, J. M. Liu, S. J. Liu and R. X. Wang, *J. Mater. Sci.*, 2021, **56**, 2451–2463.
45 W. Wang, M. Zhang, R. Mi, Y. Liu and J. Chen, *J. Alloys Compd.*, 2021, **888**, 161615.
46 B. Sun, S. Lou, W. Zheng, Z. Qian, C. Cui, P. Zuo, C. Du, J. Xie, J. Wang and G. Yin, *Nano Energy*, 2020, **78**, 105366.
47 Z. Chen, S. Fei, C. Wu, P. Xin, S. Huang, L. Selegård, K. Uvdal and Z. Hu, *ACS Appl. Mater. Interfaces*, 2020, **12**, 19768–19777.
48 B. Jiang, C. Han, B. Li, Y. He and Z. Lin, *ACS Nano*, 2016, **10**, 2728–2735.
49 J. Mujtaba, H. Sun, G. Huang, K. Mølhave, Y. Liu, Y. Zhao, X. Wang, S. Xu and J. Zhu, *Sci. Rep.*, 2016, **6**, 20592.
50 C. Yan, Y. Zhu, Y. Li, Z. Fang, L. Peng, X. Zhou, G. Chen and G. Yu, *Adv. Funct. Mater.*, 2018, **28**, 1705951.
51 J. Wang, S. Xie, L. Li, Z. Li, A. M. Asiri, H. M. Marwani, X. Han and H. Wang, *Part. Part. Syst. Charact.*, 2019, **36**, 1900109.
52 B. Wu, Y. Xie, Y. Meng, C. Qian, Y. Chen, A. Yuan, X. Guo, H. Yang, S. Wan and S. Lin, *J. Mater. Chem. A*, 2019, **7**, 6149–6160.
53 L. Zhu, F. Li, T. Yao, T. Liu, J. Wang, Y. Li, H. Lu, R. Qian, Y. Liu and H. Wang, *Energy Fuels*, 2020, **34**, 11574–11580.
54 W. Wang, Y. Yang, S. Yang, Z. Guo, C. Feng and X. Tang, *Electrochim. Acta*, 2015, **155**, 297–304.
55 H. Liu and J. Wang, *Electrochim. Acta*, 2013, **92**, 371–375.
56 S. Hao, B. Zhang, S. Ball, M. Copley, Z. Xu, M. Srinivasan, K. Zhou, S. Mhaisalkar and Y. Huang, *J. Power Sources*, 2015, **294**, 112–119.
57 J. Deng, X. Yu, Y. He, B. Lia, Q. H. Yanga and F. Kang, *Energy Storage Mater.*, 2017, **6**, 61–69.
58 Y. Sharma, N. Sharma, G. V. S. Rao and B. V. R. Chowdari, *Adv. Funct. Mater.*, 2007, **17**, 2855–2861.
59 R. A. Adams, V. G. Pol and A. Varma, *Ind. Eng. Chem. Res.*, 2017, **56**, 7173–7183.
60 B. Fan, X. Chen, A. Hu, Q. Tang, H. Fan, Z. Liu and K. Xiao, *RSC Adv.*, 2016, **6**, 79971–79977.
61 L. Guo, Q. Ru, X. Song, S. Hu and Y. Mo, *J. Mater. Chem. A*, 2015, **3**, 8683–8692.
62 A. K. Rai, T. V. Thi, B. J. Paul and J. Kim, *Electrochim. Acta*, 2014, **146**, 577–584.
63 H. Cao, X. Zhou, W. Deng, Z. Ma, Y. Liu and Z. Liu, *Chem. Eng. J.*, 2018, **343**, 654–661.
64 H. Wang, Y. Zheng, Z. Peng, X. Liu, C. Qu, Z. Huang, Z. Cai, H. Fan and Y. Zhang, *Dalton Trans.*, 2021, **50**, 7277–7283.